2011

# Comparison of GO, GO/MWCNTs composite and MWCNTs as potential electrode materials for supercapacitors

Seyed Hamed Aboutalebi
*University of Wollongong*, sha942@uowmail.edu.au

Maryam Salari
*University of Wollongong*, msalari@uow.edu.au

Konstantin Konstantinov
*University of Wollongong*, konstan@uow.edu.au

David Wexler
*University of Wollongong*

Hua-Kun Liu
*University of Wollongong*, hua@uow.edu.au

*See next page for additional authors*

Energy & Environmental Science

Cite this: *Energy Environ. Sci.*, 2011, **4**, 1855

www.rsc.org/ees

**PAPER**

# Comparison of GO, GO/MWCNTs composite and MWCNTs as potential electrode materials for supercapacitors

**Seyed Hamed Aboutalebi,[a] Alfred T. Chidembo,[a] Maryam Salari,[a] Konstantin Konstantinov,*[a] David Wexler,[b] Hua Kun Liu[ac] and Shi Xue Dou[a]**

***Received 14th January 2011, Accepted 12th March 2011***
**DOI: 10.1039/c1ee01039e**



We report the synthesis of graphene oxide/multi-walled carbon nanotube (MWCNT) composites employing an alternative and novel approach for possible application as supercapacitor materials in energy storage devices. Integrating these nanostructures resulted in a strong synergistic effect between the two materials consequently leading to a robust and superior hybrid material with higher capacitance compared to either graphene oxide or MWCNTs. Specific capacitances of 251, 85 and 60 F $g^{-1}$ were obtained for graphene oxide-multi-walled carbon nanotubes, MWCNTs and graphene oxide, respectively, in a potential range from −0.1 to 0.5 V. Most importantly, a 120% increase in capacitance was observed with increasing cycle number at 20 mV $s^{-1}$. The ease of synthesis and the exceptional electrochemical properties make the use of this nanostructure an attractive, alternative way of designing future supercapacitors in both conventional fields and new emerging areas.

## Introduction

Supercapacitor research has undergone immense growth over the last decade due to the high demand for high performing and long lasting energy devices. Much of the focus has been on increasing the energy density of these devices as they already exhibit high power density as compared to conventional batteries.

Carbonaceous materials such as carbon nanotubes, carbon aerogels, activated carbon and carbon nanofibres are some of the materials of choice used for fabrication of electrode materials.[1–4] These materials give rise to a class of supercapacitors called electrical double layer capacitors (EDLCs). EDLCs operate on a mechanism that involves non-Faradaic reactions taking place on the electrical double layer. High surface area, good conductivity and low cost of these materials have contributed to their attractiveness with carbon nanotubes playing a leading role.[5] Multi-walled carbon nanotubes (MWCNTs) have been reported to exhibit capacitance ranging from 4–135 F $g^{-1}$.[6] A major disadvantage for unfunctionalized MWCNTs has been the difficulty to disperse uniformly in any solvent as they tend to agglomerate. To solve this problem, functionalization of carbon nanotubes with nitric acid has been widely reported to boost capacitance while unfunctionalised carbon nanotubes have been sidelined due to their low capacitance.[6] To further enhance the capacitance, MWCNTs have been mixed with conducting polymers[2,7,8] and metal oxides.[9,10]

Another class of supercapacitors are the pseudocapacitors which rely on the Faradaic reactions taking place on the

[a]*Institute for Superconducting & Electronic Materials (ISEM), Innovation Campus, University of Wollongong, Wollongong, NSW, 2519, Australia. E-mail: sha942@uowmail.edu.au; Fax: +61242215731; Tel: +61242215730; konstan@uow.edu.au*
[b]*School of Materials, Mechanical and Mechateronics Engineering, University of Wollongong, Wollongong, NSW, 2519, Australia. E-mail: david_wexler@uow.edu.au; Fax: +61242215731; Tel: +61242215730*
[c]*ARC Centre of Excellence in Electromaterials Sciences, Institute for Superconducting & Electronic Materials (ISEM), Innovation Campus, University of Wollongong, Wollongong, NSW, 2519, Australia. E-mail: hua@uow.edu.au; Fax: +61242215731; Tel: +61242215730*

### Broader context

We report the synthesis of graphene oxide/multi-walled carbon nanotube (MWCNT) composites employing an alternative and novel approach for possible application as supercapacitor materials in energy storage devices. Integrating these nanostructures resulted in a strong synergistic effect between the two materials consequently leading to a robust and superior hybrid material with higher capacitance compared to either graphene oxide or MWCNTs. The dispersant free nature of the combination of these materials offers a great flexibility in the creation of high performance novel GO–MWCNT based nanocomposites with many other nanostructures (possibly metal-oxide or polymer systems). The ease of synthesis and the exceptional electrochemical properties make the use of this nanostructure an attractive, alternative way of designing future supercapacitors in both conventional fields and new emerging areas.

electrode surface. Metal oxides[3,11] and conducting polymers[12,13] are typical pseudocapacitive materials that have been vastly reported. To further enhance the capacitance, MWCNTs have been mixed with conducting polymers[2,7,8] and metal oxides.[9,10]

Graphite oxide (GO), first prepared almost 150 years ago,[14] represents an intriguing and interesting new class of carbon-based nanoscale materials with some unusual and fascinating properties that are distinct from those of other graphitic systems. GO has recently emerged as an alternative precursor offering the potential of a low cost method to fabricate graphene. The first samples of pristine graphene were deposited by mechanical exfoliation.[15] Since then, many promising applications of graphene have been introduced to put the fascinating properties of graphene to practical use, which requires the development of new routes for effective, low cost graphite exfoliation, processing and mass production with high quality.[16] Among these methods, the chemical reduction of graphite oxide, a layered material often simplistically assumed to consist of hydrophilic oxygenated graphene sheets, or graphene oxide sheets, bearing oxygen functional groups in the form of carboxyl, hydroxyl or epoxy groups on their basal planes and edges,[17,18] has been successfully used to fabricate covalently functionalized single-layer GO.[19] The presence of these oxygen-containing functional groups provides potential advantages for numerous applications, mainly because they can be used to introduce multifunctionalities,[18] which are responsible for the solubility of graphene oxide in water and other solvents.[20] Recently graphene has received great attention as a possible electrode material for lithium ion batteries[21,22] as well as supercapacitors.[23–25] Capacitances as high as 135 F $g^{-1}$ have been reported by Stoller *et al.*[26] Composites of graphene oxide and metal oxides such as ZnO[27] and $MnO_2$[28] have also been reported over the last year with capacitances as high as 197.2 F $g^{-1}$. Although some attempts have been made to combine CNTs and GO or reduced GO (rGO),[29–33] the use of functionalized CNTs or complicated procedures employed in these methods quite effectively reduces the practicality and reproducibility in everyday use.

The present paper addresses the above-mentioned issue by introducing a facile method based on the amphiphilic properties of GO and reports the highest recorded capacitance values reported for GO or hybrid materials of GO–MWCNTs, which are even higher than the values reported for GO–metal oxide composites. These results offer a novel yet simple and effective way of designing advanced materials with extraordinary properties by incorporating two different materials neither one of which alone might be essentially perfect for the required applications. It is suggested that the synergistic effect of the combination of these materials combined with the preferential electro-reduction of GO gives rise to these remarkable values.

## Experimental procedure

1 g of natural graphite flakes (Asbury Graphite Mills, US) was thermally expanded at 1050 °C for 15 s. The final expanded graphite (EG) was then used for the production of GO. 1 g of EG and 200 ml of sulfuric acid ($H_2SO_4$, 98%, Merck) were mixed and stirred in a three neck flask. Next, 5 g of $KMnO_4$ was added to the mixture while stirring. The mixture was then stirred at 30 °C for 24 h. Next, 200 ml of de-ionized water and 50 ml of $H_2O_2$ were poured slowly into the mixture changing the colour of the suspension to light brown. Having stirred for another 30 min, the GO particles were then washed and centrifuged with HCl solution (9 : 1 vol water : HCl) three times, then centrifuged again and washed with de-ionized water until the pH of the solution became about 5 to 6. The obtained GO particles were then diluted using DI water (~1.8 mg $ml^{-1}$) and delaminated just by gentle shaking.

For the dispersion experiments, carbon nanotubes (CNTs, Sigma, multiwalled, diameter between 6 and 13 nm) powder was added into 25 ml of diluted GO dispersion in water with a mass ratio of 1 : 3 (CNT/GO). Then the dispersion was sonicated for 30 min using a conventional bath sonicator followed by 30 min sonication in an ultrasonicator (Sonics, VC505, 500 watts, tip diameter 13 mm). A maximum amplitude of 40% was employed for CNT samples, respectively. Almost the same route is reported in a recent paper to disperse SWCNTs with GO in water.[34]

The morphology of GO samples was examined by a scanning electron microscope (JSM 7500F, JEOL). Gold sputtering was avoided because the gold layer to be deposited on GO film surface is usually too thick (2–20 nm), making GO layers undetectable. Thus the insulating GO sheets were examined directly without further sputtering. Images were acquired by secondary electron and transmission electron detectors employing dark field and bright field imaging techniques, which allowed high throughput examination of GO sheets over the millimetre scale areas. However, because the GO layer was deposited on the insulating $SiO_2$/Si substrate and no Au coating was deposited to avoid charge, it was rather inevitable to find some burnt spots and unwanted carbonaceous contamination, especially when high acceleration voltages or short working distances were used.

To measure the interlayer spacing of the materials, X-ray diffraction experiments were performed at room temperature using a high resolution X-ray diffraction system (XRD; GBC MMA) employing Cu K$\alpha$ radiation (X-ray wavelength $\lambda = 1.5406$ Å operating at 40 keV, a cathode current of 30 mA) under normal laboratory conditions in thin film configuration. To prepare the samples, droplets of the suspensions were dried in air on quartz substrate. For optical absorbance measurements, the GO–MWCNT in water, GO dispersion in water and CNT dispersion in water were diluted and measured on a UV-VIS spectrometer (Shimadzu, UV-3600 UV-VIS-NIR). $\zeta$ potential measurements were conducted using a $\zeta$ potential measurement instrument (Malvern, Zetasizer) at room temperature. Raman spectroscopy (Horiba JobinYvon/LabRAM HR) was used to analyse the samples using a 632.8 nm laser. The elemental composition was characterized using the X-ray photoelectron spectroscopy (XPS, PHOIBOS 100 hemispherical analyser, SPECS GmbH) with a pass energy of 26.00 eV, 45° takeoff angle and a beam size of 100 μm. In the case of cycled electrodes, the electrodes were dried in an oven at 80 °C prior to XPS.

The working electrode was prepared by coating the active material onto stainless steel sheets (1 cm × 1 cm) previously polished with sand paper and ultrasonicated in ethanol for an hour. 7 mg of active material (MWCNT–GO, GO, and MWCNT) were mixed with 2 mg of carbon black and 1 mg of PVDF binder (ratio 7 : 2 : 1) in an agate mortar in NMP (*N*-methyl pyrrolidinone) solvent and ground using a pestle. The resulting slurry was then spread onto the polished stainless steel

 

surface and allowed to dry in a vacuum oven for 24 hours. The end loading of active material for each electrode was 1 mg $cm^{-2}$.

Electrochemical experiments were performed on the CHI660C (CH Instruments, Inc) electrochemical workstation using the three electrode system in a beaker type cell at room temperature. An electrolyte solution of 1 M $H_2SO_4$, a silver/silver chloride reference electrode and a platinum foil as a counter electrode were used. Cyclic voltammetry (CV) was performed over a voltage range of −0.2 to 0.5 V at various scan rates (5 to 100 mV $s^{-1}$) with specific capacitance being calculated at the lowest scan rate of 5 mV $s^{-1}$. Another method used to calculate capacitance, chronopotentiometry, was performed at varying current densities (0.4 to 8 $Ag^{-1}$) over a potential window range from −0.1 to 0.5 V. The highest specific capacitance was recorded at 0.4 $Ag^{-1}$ for charge/discharge (CD). Electrochemical Impedance Spectroscopy (EIS) measurement was carried out between 10 kHz and 0.01 Hz using a 5 mV rms sinusoidal modulation at a bias potential of 0.2 V.

## Results and discussion

### Structural characterization

The suspension of GO in water exhibited clear anisotropy in its texture even after gentle shaking, which is typical for graphene sheets with large sizes and high aspect ratios.[16] Inspired by the amphiphilic properties of GO,[32] GO was employed as a molecular dispersing agent to process MWCNTs in water in order to make a hybrid material, GO–MWCNTs. The size dependent amphiphilic properties of GO offer a simple way to engineer the structure and fine tune its amphiphilicity, which therefore makes it an ideal candidate as a water processable material. The basal plane of GO consists of many π-conjugated aromatic domains which in theory can strongly interact with the surface of CNTs through π–π attractions.[32] There are also some earlier reports on the adsorption of drug or dye molecules through π–π interactions.[35,36] The dispersion of GO/CNT remained stable for some days. Although a small portion of the suspended CNTs eventually settled down, a gentle shaking was more than enough to readily redisperse the suspension. Fig. 1 shows the X-ray diffraction patterns of the samples of both GO and GO mixed with MWCNTs sample.

The X-ray pattern of the as-prepared GO shows a distinct peak at 10.76° corresponding to a layer-to-layer distance (*d*-spacing) of about 8.22 Å for a typical sample which is due to an approximately one-molecule-thick layer of water trapped and presumably hydrogen-bonded between the graphene oxide sheets.[37] This peak is typical of graphene oxide materials and depends on both the method of preparation and the level of humidity. However, the introduction of MWCNTs downshifts the peak to 1.152° which is analogous to a *d*-spacing of about 70.88 Å demonstrating an increase in the space between the layers. For XRD, the interlayer spacing of the materials is proportional to the degree of oxidation. The XRD pattern further proves the complete oxidation of graphite intercalated compound (GIC) samples. Moreover, the mean crystallite size of GO sheets in the dried suspension that are oriented perpendicularly to the diffracting plane was calculated from the full width at half maximum (FWHM) of the X-ray diffraction peak using the Scherrer's equation, and was found to be 4.05 ± 0.13 nm. Fig. 2 shows the X-ray photoelectron spectra of both samples. The spectra for the C region demonstrate the $sp^2$ hybridized C1s peak attributed to the pristine graphene at 284.7 eV with its well-known asymmetric line shape.

The C1s spectra were compared in both samples by deconvoluting each spectrum into three peaks that correspond to the following functional groups: carbon $sp^2$ (C=C, 284.8 eV), carbon $sp^3$ (285.6 eV), epoxy/hydroxyls (C–O, 286.2 eV), and carboxylates (O–C=O, 289.0 eV). Carbon $sp^2$ and carbon $sp^3$ peaks are overlaid and indicated as carbon–carbon bonds. Substantial changes can be observed in the C1s spectra collected after the introduction of MWCNTs, and the C1s spectrum is where the most significant change is observed. The X-ray photoelectron spectroscopy (XPS) analysis (Fig. 2) demonstrates that the ratio of carbon–carbon bonds to epoxy/hydroxyls and carboxylate groups increases remarkably after the introduction of MWCNTs into the structure, implying an efficient addition of carbon groups during the fabrication process and a simultaneous increase in $sp^2$ C–C bonds which is an indication of graphitic carbon.[38]

A major issue during Raman spectroscopy is the sample damage induced by laser heating because of the fact that GO could undergo local decomposition when irradiated with focused laser spots even at moderate power levels.[39] It is well known that the G band is assigned to the first-order scattering of the $E_{2g}$

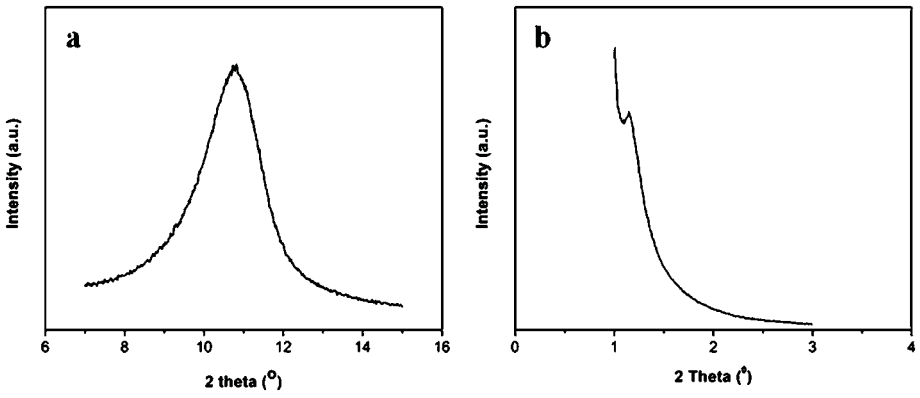


**Fig. 1** XRD patterns of (a) GO and (b) GO mixed with MWCNTs sample.

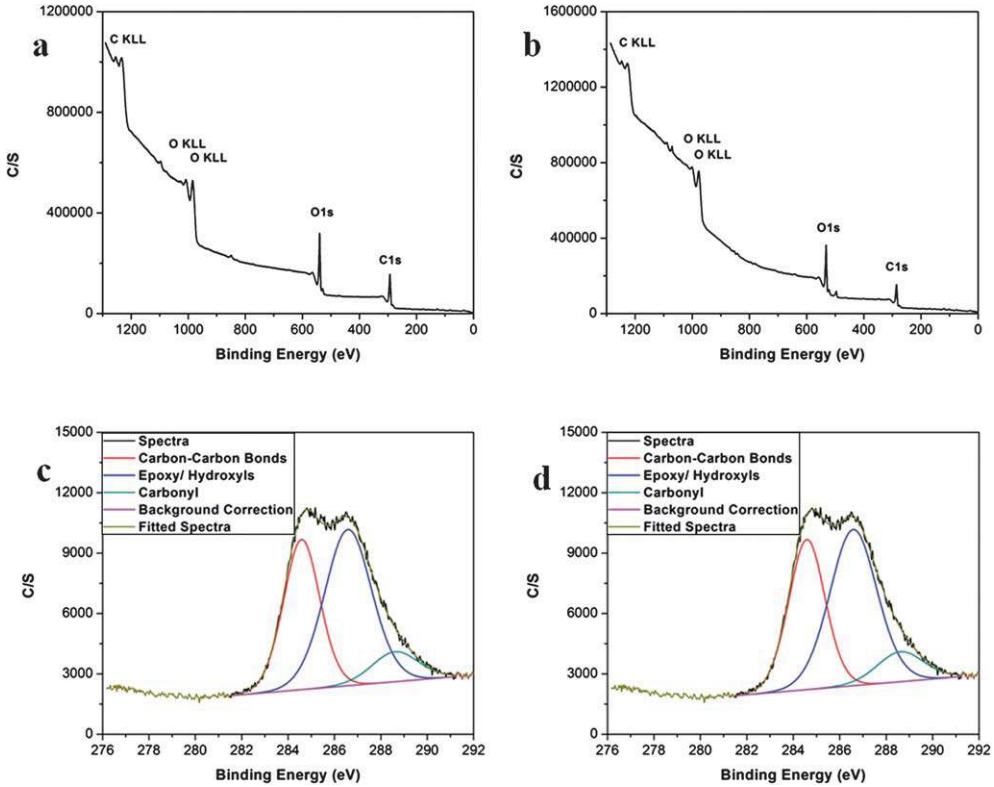


**Fig. 2** XPS spectra of (a) GO, (b) GO–MWCNTs, (c) fitted spectrum of GO in carbon region and (d) fitted spectrum of GO–MWCNTs in carbon region.

mode observed for $sp^2$ carbon domains and a pronounced D band is associated with disordered structural defects (*e.g.*, amorphous carbon or edges that can break the symmetry and selection rule). The Raman spectra shown in Fig. 3 indicate a total decrease of the $I$(D)/$I$(G) ratio upon the introduction of MWCNTs as well as a red shift of the peak positions.

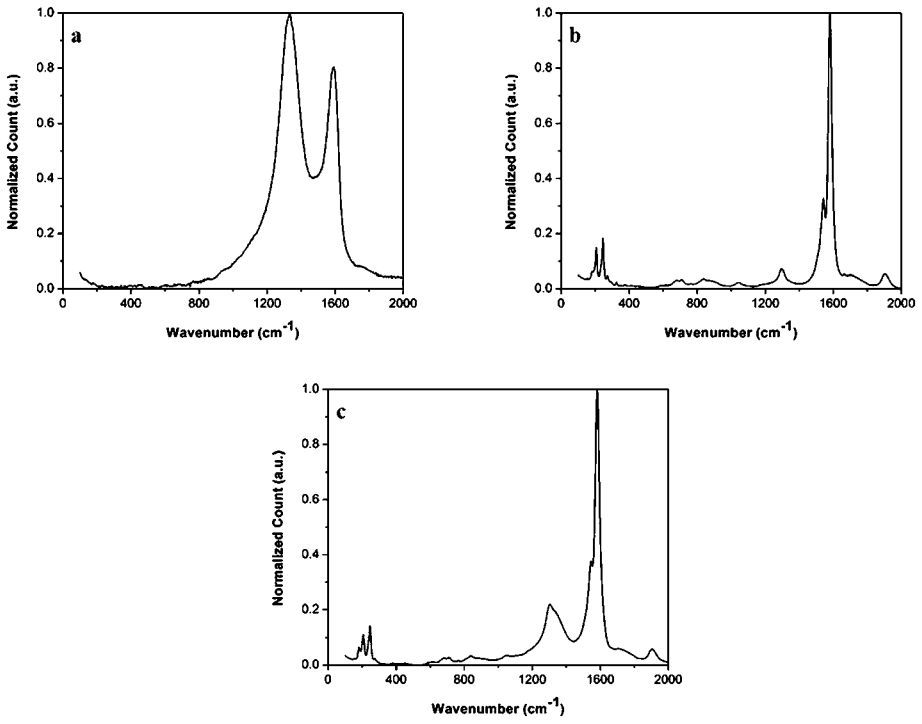


**Fig. 3** Raman spectra of (a) as-prepared GO, (b) pristine MWCNTs and (c) GO–MWCNTs.

 

Moreover the Raman spectrum of MWCNTs shows a distinct radial breathing mode (RBM) feature at low frequencies and a tangential (G-band) multi-feature at higher frequencies which is typical of both SWCNTs and DWCNTs but also can be observed in the case of the present MWCNTs serving as a sign that the innermost diameter is less than 2 nm. Since the low-frequency region is considered a silent region in the case of other carbon materials, the peaks should be attributed to the thin tubes with a diameter less than 2 nm which is typical for MWCNTs fabricated by employing the arc synthesis method. It might also originate from the so-called coupled breathing-like modes (BLMs) as predicted by Popov *et al.*, rather than individual RBMs. These structural features can also be observed in the case of the hybrid material albeit with a significant change in the position and intensity of the pronounced D peak.

Fig. 4 presents the UV/Vis spectra of both as-prepared GO suspensions and the GO mixed with MWCNTs. The peak in the UV/Vis spectrum of GO in the region of 227–231 nm determines the degree of remaining conjugation ($\pi$–$\pi^*$ transition).[40,41] The shoulder around 300 nm can be ascribed to the n–$\pi^*$ transition of carbonyl groups.[40] While almost no structural peaks can be observed in the case of MWCNTs suspended in sodium dodecyl sulfate (SDS), as shown in Fig. 4, another absorption peak at 205 nm, beside the pristine GO dispersion peak at 231 nm, can be seen in the mixture indicating $\pi$–$\pi$ attractions between the surface of the CNTs and the basal planes of GO further strengthening the hypothesis that the $\pi$-conjugated aromatic domains of the GO have interacted with the surface of the CNTs.

The UV/Vis results demonstrate that the suspension of MWCNTs can be effectively stabilized using GO sheets. The ionization of oxygen groups typically leads to high stability of a GO aqueous dispersion. Considering the case of GO platelets, which are flexible in nature unlike hard disks, the interparticle interaction is completely based on the charge stabilization and double layer extension.[42] To better illustrate this point, $\zeta$ potential study was carried out on GO and the hybrid material. $\zeta$ potential confers the degree of repulsion between charged particles in a dispersion. Therefore, a high $\zeta$ potential is an indicator that the dispersion resists aggregation and consequently remains stable. A $\zeta$ potential study of GO and the hybrid material reveals that GO sheets are negatively charged which results in high charge density and consequently high hydrophilicity of the GO sheets significantly increasing the colloidal stability.

In contrast, pristine MWCNT dispersions in water are not stable and tend to agglomerate. However, in the case of the hybrid material, the $\zeta$ potential becomes significantly more negative (from −39 to −49 mV) suggesting higher stability of the mixed solution. The higher $\zeta$ potential implies higher electrostatic repulsion and reduced overlapping areas. This, in turn, supports the view that the hydrophobic domains in the basal plane of GO have strongly interacted with the hydrophobic surface of MWCNTs through $\pi$–$\pi$ attractions. Although both particles are negatively charged, the negative groups are mostly located on the edges of GO leaving behind hydrophobic graphitic islands which can interact with the hydrophobic surface of MWCNTs forming a hybrid structure.

In order to observe and assess the structural morphology of the hybrid material, scanning transmission electron microscopy (STEM) was employed. Fig. 5 presents the corresponding SEM, STEM and dark field micrographs of the as-prepared GO–MWCNT sample, which is in good agreement with the

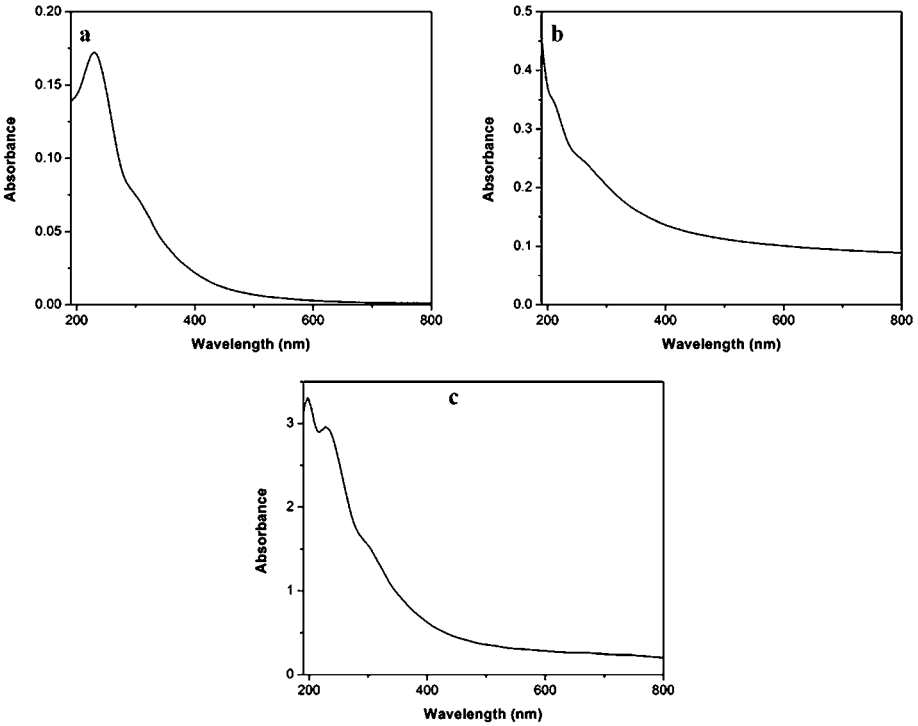


**Fig. 4** UV/Vis spectra of (a) as-prepared GO dispersion, (b) MWCNTs and (c) GO mixture with MWCNTs.

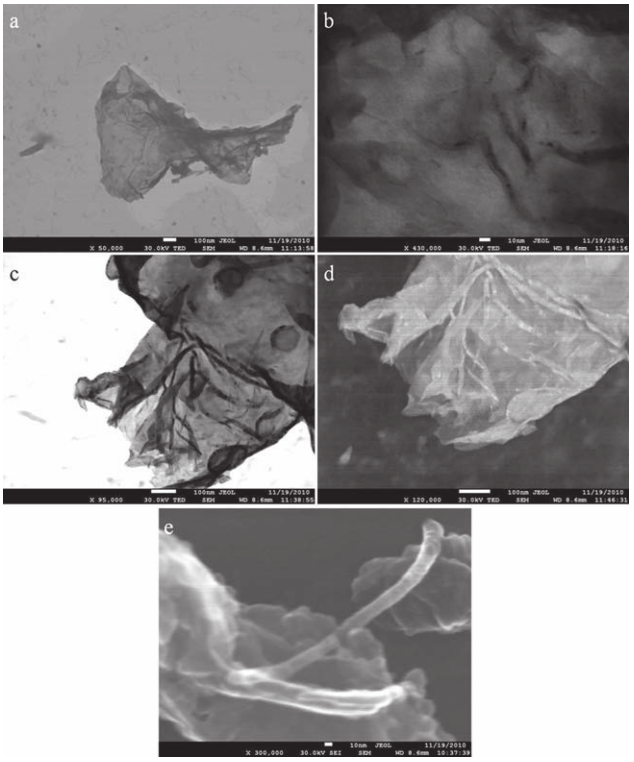


**Fig. 5** (a) STEM micrograph of an isolated GO–MWCNT, (b) high resolution STEM image showing MWCNTs, (c) STEM micrograph of MWCNTs on the surface of an isolated GO sheet, (d) dark field micrograph of the same sheet, better revealing the MWCNTs, and (e) SEM micrograph of an isolated MWCNT acting as a bridge between GO sheets.

results obtained from UV/Vis and ζ potential measurements. The micrographs demonstrate that MWCNTs are adsorbed on the islands on the surface of GO and not on the edges which are typically hydrophilic. Also, the dark field imaging technique proved to be useful to illustrate the faint features of MWCNTs on the surface of GO. The fragmentation and breakage of GO sheets is also observed which is inevitable due to the breakage during the sonication process.

The Raman spectra shown in Fig. 6 indicate an enhancement of the D peak upon the electrochemical reduction of GO as well as a shift of the D peak position. Although a prominent D peak is typically an indication of disorder in the Raman spectrum of carbon materials and there are some reports on the decrease of $I$(D)/$I$(G) ratio,[43] our observations are consistent with previous reports on reduced GO (rGO). The same phenomenon was observed by Ruoff *et al.*,[44] Ajayan and coworkers,[45] *etc.*[46–49] This strong D peak observed in rGO should be further investigated. However, Ajayan and coworkers had concluded that these defects might be due to the smaller size of the graphene sheets as well as the remaining functionalities.[45] This enhancement of the D peak might also be due to the decrease in the size of the newly formed graphene like $sp^2$ domains, which are smaller than the domains in the initial sample before electrochemical reduction.[44] Ferrari *et al.*,[50] also proposed that GO is in an amorphous state and that a graphite-like state is only recovered after reduction, implying that the $I$(D)/$I$(G) ratio cannot be directly compared between the two states.

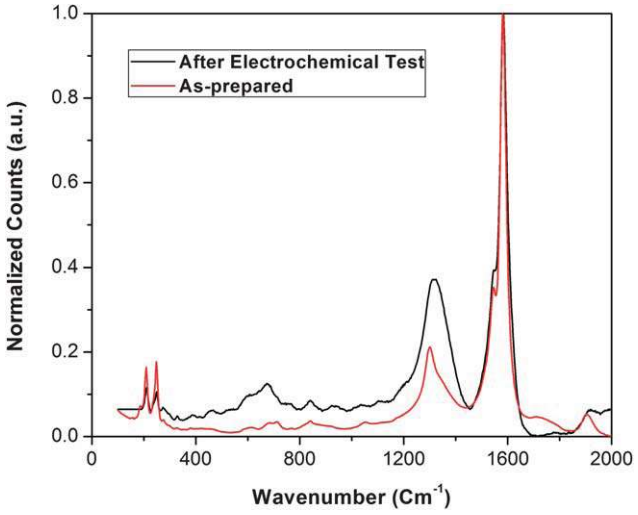


**Fig. 6** Raman spectra of as-prepared electrode and the same electrode after the electrochemical tests.

## Electrochemical characterization

Cyclic voltammetry (CV) is usually the first method used for diagnostic testing of supercapacitor performance (Fig. 7). The specific capacitance of the three electrodes was therefore calculated using the following formula.

$$C_s = \frac{1}{mv(V_a - V_c)} \int_{-0.2}^{0.5} I(V)\mathrm{d}V \qquad (1)$$

where $m$ is the mass of the active material, $v$, the scan rate, $(V_a - V_c)$ represents the potential window and the integral area under the cyclic voltammograms.

The calculated specific capacitances for GO–MWCNT, MWCNT and GO were recorded to be 251, 85 and 60 F $g^{-1}$ respectively. These results are consistent with the range of 15 to 80 F $g^{-1}$ expected for MWCNTs reported in the literature by Frackowiak *et al.*[51,52] and much higher than the 10.9 F $g^{-1}$ for GO[53] possibly due to a much larger size of the GO sheets employed here (1–2 orders of magnitude).

Fig. 7(a) shows cyclic voltammograms for the MWCNTs, GO and GO–MWCNTs composite electrodes recorded at 5 mV $s^{-1}$. MWCNTs typically show an almost rectangular cyclic voltammogram while a distorted rectangular shape is observed for the GO and GO–MWCNT composite due to the pseudocapacitance behaviour originating from oxygen groups on the surface of the GO. No peaks were observed for the MWCNTs electrode as would be expected for carbon material showing classically the double layer capacitor behaviour. However, a broad peak characteristic of carbon material with oxygen groups is observed between 0.4 and 0.5 V for the GO–MWCNT electrode (Fig. 7 (a)). The peak can be attributed to the transition between quinone/hydroquinone groups on the carbon material.[54] The shape of the CV curve for the GO–MWCNTs composite is maintained even at a high scan rate of 100 mV $s^{-1}$ (see Fig. 7(b)) indicating the good capacitive behaviour, rapid diffusion of electrolyte ions from the solution into the pores of the modified electrode[55] and low ESR. The data obtained for Fig. 7(a) also

 

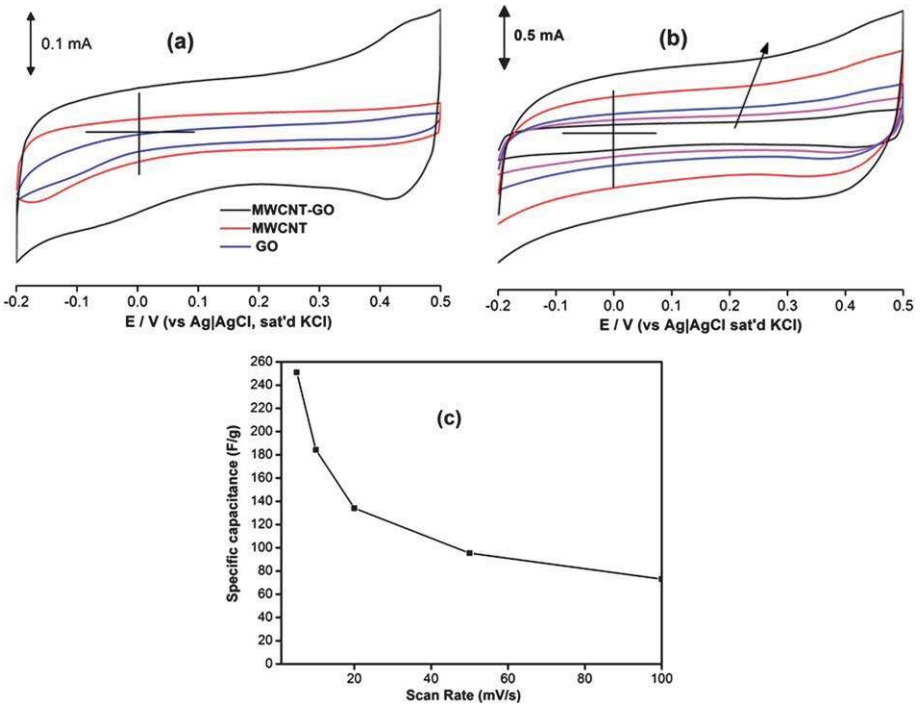


**Fig. 7** (a) Comparative cyclic voltammograms for GO–MWCNTs, MWCNTs and GO at 5 mV $s^{-1}$, (b) scan rate studies for GO–MWCNT in 1 M $H_2SO_4$ at 5, 10, 20, 50 and 100 mV $s^{-1}$, as indicated by the arrow. (c) Variation of specific capacitance with scan rate for GO–MWCNTs.



yielded a linear relationship between the current and the scan rate indicative of a surface-bound redox system. A possible explanation of this phenomenon could be the high conductivity of the two constituent materials coupled with the high porosity of the electrode material which results in a synergistic behaviour of the material and allows penetration by electrolyte ions to the electrode surface as supported by the shape of the CV curve at a high scan rate. MWCNTs can act as conducting wires between the graphene oxide sheets providing a conductive path for movement of electrons. Graphene oxide sheets are well known to agglomerate resulting in a smaller surface area accessible for ion exchange and electrical double layer. A mixture of carbon nanotubes and the graphene sheets results in an increase in the space between the layers as explained earlier by the XRD results. This enhances capacitance by increasing the effective surface area for charge storage and channels for ion exchange. Therefore, CNTs act effectively as a spacer and inhibit the restacking of graphene oxide sheets and therefore facilitate the diffusion of electrolyte. Furthermore, a recent theoretical study revealed that for cylinders with radius less than 20 nm, increase in double layer capacitance can be observed, providing an enhanced electrochemical driving force for electron transfer and a possible partial cause for altered electrode kinetics at carbon nanotube modified electrodes.[56] Small CNTs are therefore expected to afford higher energetic driving force for electron transfer. This effect can be more pronounced in the case of individual and fully separated CNTs entangled between GO sheets. Bundling of CNTs can inhibit the diffuse double layer to extend further into the solution, however, based on the SEM pictures, no bundling of CNTs can be observed in our case which might be partially responsible for the observed enhancement in capacitance. It is proposed that a combination of these factors might be responsible for the observed synergistic effect.

The highest specific capacitance for the composite was recorded at 5 mV $s^{-1}$ and decreased steadily with increasing scan rate as is usually expected due to diffusion limitations in the pores on the electrode surface as shown in Fig. 7(c).

Galvanostatic charge–discharge (CD) was performed on the three electrodes in a potential window from −0.1 to 0.5 V to give a more accurate measurement of the capacitance. Fig. 8(a) shows the charge–discharge profiles of the MWCNT, GO and GO–MWCNT electrodes at a current density of 0.4 $Ag^{-1}$. A common feature of the three electrodes is the linear charging and discharging profiles indicating purely capacitive behaviour. Furthermore, the electrodes showed no observable IR drop. The specific capacitance was calculated using eqn (2):

$$C = \frac{i \times \Delta t}{m \times \Delta E} \quad (2)$$

where $i$ is the discharge current, $\Delta t$, the discharge time, $m$, the mass of the active material and $\Delta E$, the potential window. The specific capacitances calculated from the charge–discharge profiles in Fig. 8(a) were 181, 36 and 20 F $g^{-1}$ for GO–MWCNT, MWCNT and GO respectively. The higher capacitance of the composite can be attributed to the improvement in conductivity and good dispersion of the MWCNTs in the presence of GO.

The results are in agreement with those calculated using cyclic voltammetry where a synergistic effect between the GO and MWCNTs is observed. However, the recorded values here are lower than those obtained using cyclic voltammetry. Fig. 8(b) shows the variation of specific capacitance with current density. A sharp decrease in specific capacitance is observed at low

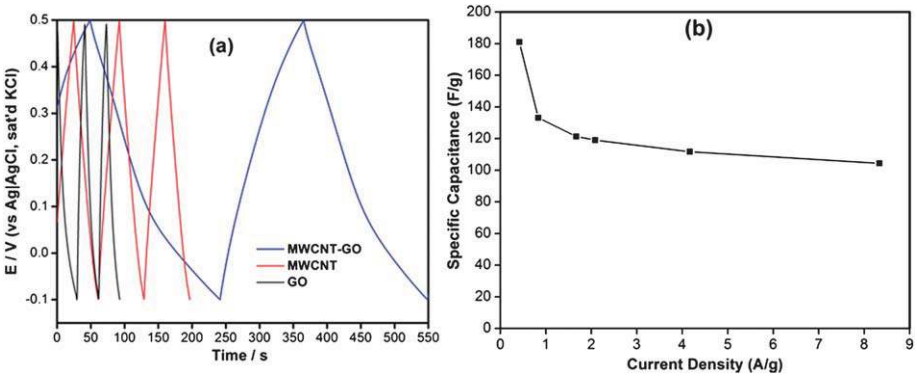


**Fig. 8** (a) Charge–discharge curves for GO–MWCNTs electrode on stainless steel at 0.4 $Ag^{-1}$. (b) Specific capacitance as a function of current density in 1 M $H_2SO_4$.



current densities but decreases steadily at higher current densities indicating good power capability of the electrode. The decrease could be attributed to the decreased access to the active surface by ions as current density increases.

Electrochemical impedance spectroscopy is a powerful technique that gives a wealth of information regarding internal resistance of the electrode material and resistance between the electrode and the electrolyte. We therefore performed electrochemical impedance measurements from 10 kHz to 10 mHz at a potential of 0.2 V *vs.* Ag|AgCl reference electrode (Fig. 9). Nyquist and Bode plots for the three electrodes were plotted and analysed. To better understand the processes taking place on the electrode surface we divided the interpretation of these data into two regions, the high frequency and the low frequency regions.

At high frequency, the intercept between the impedance plot and the real impedance ($Z'$) axis gives the magnitude of the solution resistance (Rs) of the cell. The solution resistance for the three materials was very low at 0.91, 1.17, and 1.17 Ω for the MWCNT, GO and GO–MWCNT. Another interesting feature in the high frequency region is the semicircle observed for the MWCNT and GO–MWCNT electrodes. The impedance experiment was performed on all three electrodes after 20 cycles to activate the electrode materials, which explains the presence of the semicircle which was not present at the beginning of the stability tests in Fig. 9(b). Charge transfer resistance represents the electrode resistance and is closely related to the surface area and conductivity of the electrode. The diameter of the semicircle in the high frequency region gives an indication of the charge transfer resistance ($R_{CT}$). The MWCNTs electrode recorded an $R_{CT}$ of 5.13 Ω and no semicircle was observed for the GO electrode due to the good conductivity of the material. A combination of these two materials resulted in the lowering of the charge transfer resistance in the GO–MWCNT electrode (1.12 Ω) implying lower resistance to ion movement from the pores of the composite. The synergistic effect of the MWCNT and GO electrodes is therefore apparent from the Nyquist plot, and from the CV and CD data in Fig. 7(a), 8(a) and 9(a).

At low frequencies, supercapacitor electrodes exhibit typical capacitive behaviour, where an almost vertical line is observed on the Nyquist plot and a phase angle close to 90° on the Bode plot (Fig. 9). MWCNTs and GO are known to exhibit almost ideal capacitance and this is confirmed by the phase angle almost reaching 90°. However, the slope on the Nyquist plot deviates from a perfect vertical line possibly due to pseudocapacitance effects from the oxygen groups on the GO. A purely capacitive element ($C_{dl}$) was therefore replaced by a constant phase element (CPE) in the electrical equivalent circuit to obtain a good fit with low relative errors.

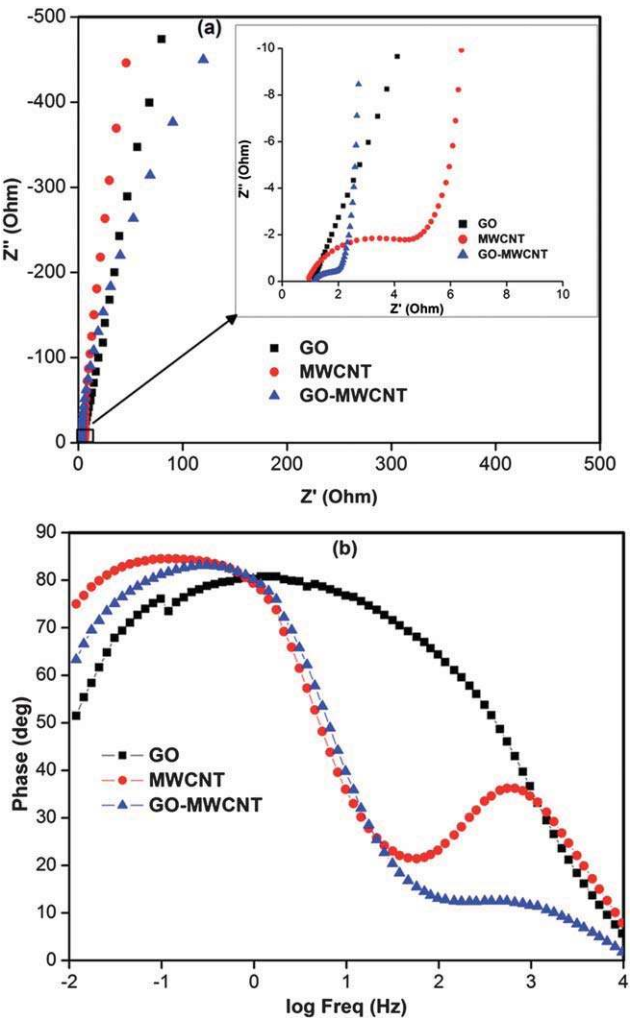


**Fig. 9** (a) Nyquist plot for GO–MWCNT composite (inset: magnified high frequency region). (b) Bode angle plot for the composite.

**Table 1** Equivalent circuit parameters for the MWCNT–GO composite electrode

| Element | Value | Error (%) |
|---|---|---|
| R1/Ω | 1.17 | 1.14 |
| Q1/mF | 14.04 | 21.91 |
| n1 | 0.85 | 3.23 |
| R2/Ω | 1.12 | 4.21 |
| Q2/mF | 0.0086 | 3.7187 |
| n2 | 0.97 | 0.75 |
| R3/Ω | 164.09 | 5.38 |

$$Z_{CPE} = \frac{1}{[Q(j\omega)^n]} \quad (3)$$

where $Q$ is defined as the frequency independent constant relating to the surface electroactive properties, $\omega$ is the radial frequency; the exponent $n$ arises from the slope of log $Z$ *vs.* log $f$. The value of $n$ varies between $-1$ and 1. When $n = 0$, the CPE represents a pure resistor. At $n = 1$, a pure capacitor and an inductor at $n = -1$. At $n = 0.5$, the CPE corresponds to Warburg impedance ($Z_W$). Two CPE elements were defined to cater for the deviation from ideal capacitor behaviour.[57] The values of $n$ for the two CPEs are both very close to 1 which denotes a pure capacitor, implying highly capacitive behaviour by the electrode. The presence of the CPE also indicates the porous nature of the electrode as explained by Girija and Sangaranarayanan.[58] R1 and R3 represent the solution resistance and the ionic resistance through the electrode material, respectively, while R2 is the charge transfer resistance. The values of all the other fitting elements from the modified Randles circuit are shown in Table 1, including the error values. Electrical equivalent circuit used in fitting the experimental EIS data obtained from the GO–MWCNT electrode is also given in Fig. 10.

Stability studies were performed for the GO–MWCNT using cyclic voltammetry and EIS. An interesting phenomenon was observed where the specific capacitance increased significantly with increasing cycle number as shown in Fig. 11(a).

The electrode was cycled for 1000 times at a scan rate of 20 mV $s^{-1}$. In the first 100 cycles, the rapid increase in the capacitance can be attributed to the activation of the electrode material and electrochemical reduction of the GO. In the second segment starting from 100 to 1000 cycles, a steady increase in capacitance is observed possibly due to the depletion of oxygenated groups on the electrode surface as the reduction of GO progresses. This is supported by the XPS spectra in Fig. 12. The loss of oxygen functionality is clearly evident in the core C1s spectra (Fig. 12). However the high energy tail at 289.7 eV suggests that some residual oxygen functionalities (mainly carboxylates) still remain even after the electrochemical reduction of GO.

It is usually assumed that employing MWCNTs in composite or hybrid materials leads to low percolation thresholds, meaning very little material is needed for conduction. Thus, even a small amount of CNTs is capable of delivering higher conductivity through the system. Therefore, MWCNTs can channel electrical current to some preferential sites on the surface of GO, providing that the electrical current passes through the GO layers, and thus GO is partially reduced to rGO upon deoxygenation of GO. Joule heat generated during the application of current through GO might make it possible to reduce GO to rGO. GO is essentially a water absorbent compound. As a result, hydroxyl groups which are highly reactive can be readily ionized to give out $H^+$ with the presence of water. Therefore, the existence of this absorbed water favours the reduction of GO.[59,60] Based on the XPS results, the amount of hydroxyl groups decreases

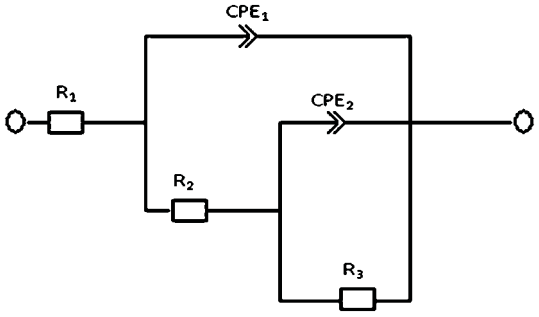


**Fig. 10** Electrical equivalent circuit used in fitting the experimental EIS data obtained from the GO–MWCNT electrode.

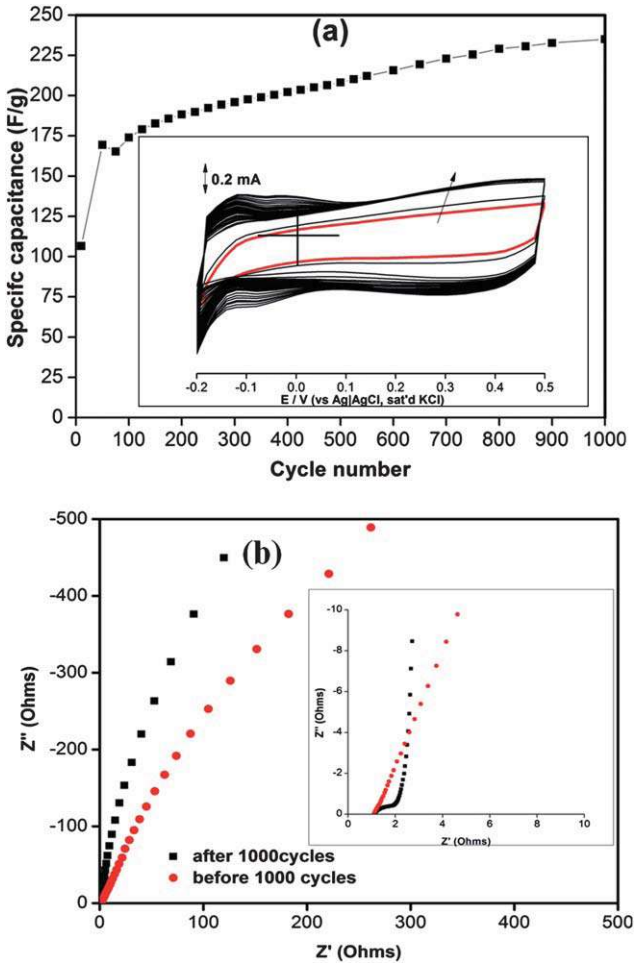


**Fig. 11** (a) Change in specific capacitance with increase in cycle number, calculated from cyclic voltammetry data at 20 mV $s^{-1}$. Inset shows the growth of CV's with increase in cycle number. (b) Comparative Nyquist plots before and after 1000 cycles.

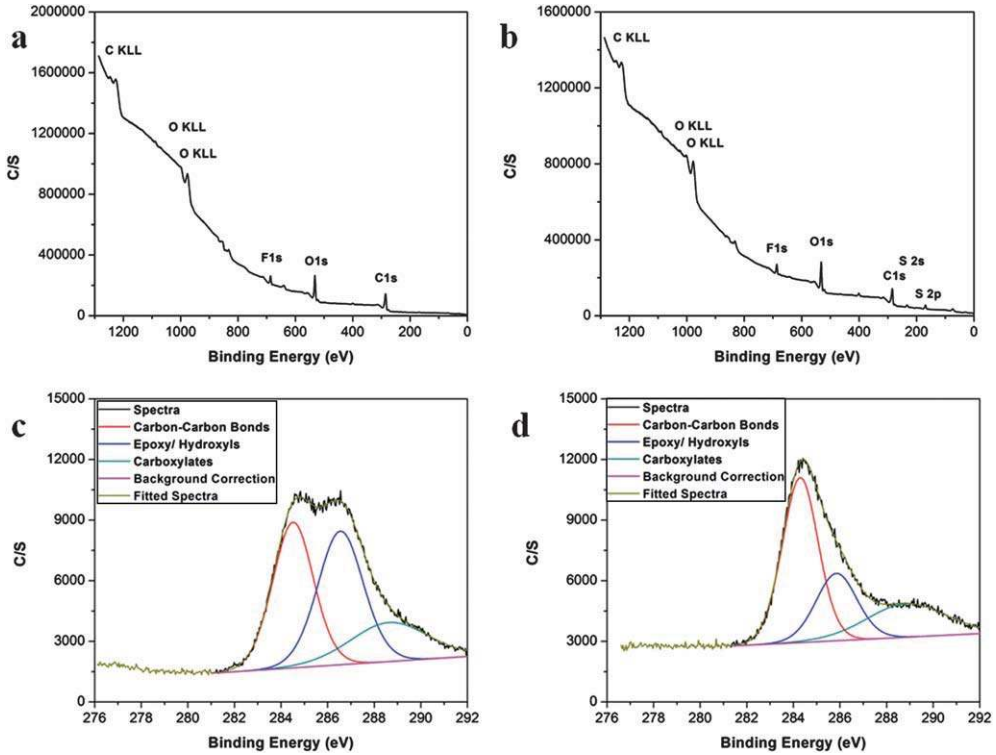


**Fig. 12** XPS spectra of (a) as-prepared electrode, (b) the same electrode after the electrochemical tests, (c) fitted spectra of as-prepared electrode in carbon region and (d) fitted spectra of the same electrode after the electrochemical tests in carbon region.



dramatically after the reduction of GO which might be considered as a consequence of the protonation involved in the electroreduction process, which is known to be facilitated at lower pH values.[60]

$$GO + aH_3O^+ + be^- \rightarrow rGO + cH_2O \quad (4)$$

A total increase in specific capacitance by 120.5% is recorded in 1000 cycles reaching a maximum of 235 F $g^{-1}$ at 20 mV $s^{-1}$. Cycling of the GO–MWCNT composite in $H_2SO_4$ contributed to the reduction of GO to reduced graphene oxide (rGO) and hence an increase in capacitance. A similar trend has been reported by Shao *et al.*[61] and Chen *et al.*[54] It is interesting to note that in the presence of MWCNTs, the peak at ~−0.1 V continues to grow with increase in the number of cycles. This could possibly have been due to the MWCNT having a catalytic effect on the reduction of GO and intercalation of sulfur in the pores.

Due to this peculiar phenomenon observed with the increase in the CV area for the GO–MWCNT electrode, we performed electrochemical impedance spectroscopy and XPS after cycling. From the XPS (Fig. 12), we observed a significant increase in the ratio of carbon–carbon bonds to epoxy/hydroxyls and carboxylate groups (from 0.65 to 1.09) after the electrochemical reduction of the electrode. Finally, a peak attributing to sulfur (S2p) which can be in the form of either $HSO_4^{-1}$ or $SO_4^{-2}$, corresponding to 6.98 at% sulfur on the surface of the sample, can be observed suggesting the accumulation of sulfur during the electrochemical reduction of the prepared electrode.

In the high frequency region, of the Nyquist plot, a semicircle was observed after 1000 cycles but was not detected before cycling. A plausible explanation could have been an increase in charge transfer resistance with increase in cycle number due to intercalation of ions on the electrode surface between GO layers as shown by the XPS spectra where the amount of sulfur ions intercalated between GO layers increased to 6% as previously discussed. The cyclic voltammograms also change the shape with increase in scan number becoming more rectangular (see Fig. 11 (a), inset).

## Conclusions

In conclusion, we have demonstrated the feasibility of designing a new generation of hybrid electrochemical supercapacitors for use in advanced energy devices based on the synergistic behaviour of GO–MWCNT electrodes. The dispersant free nature of the combination of these materials offers a great flexibility in the creation of high performance novel GO–MWCNT based nanocomposites with many other nanostructures (possibly metal-oxide or polymer systems). The hybrid nanostructured material demonstrates a strong synergistic effect leading to higher capacitance compared to either graphene oxide or MWCNTs. The mixture of GO–MWCNT showed exceptional stability due to the π–π interactions between the two carbonaceous materials. A maximum capacitance of 251 F $g^{-1}$ was observed at 5 mV $s^{-1}$ and a total increase of 120.5% was recorded in 1000 cycles for the hybrid material at a scan rate of 20 mV $s^{-1}$. It is assumed that MWCNTs can channel the electrical current to some preferential sites on the surface of GO resulting in a partial recovery of GO to rGO.

## Acknowledgements

The authors thank the Australian Research Council for the financial support provided through DP (1093952). The authors thank Dr T. Silver for critical reading of the manuscript.

## References

1 A. T. Chidembo, K. I. Ozoemena, B. O. Agboola, V. Gupta, G. G. Wildgoose and R. G. Compton, *Energy Environ. Sci.*, 2010, **3**, 228–236.
2 S. C. Canobre, D. A. L. Almeida, C. Polo Fonseca and S. Neves, *Electrochim. Acta*, 2009, **54**, 6383–6388.
3 V. Khomenko, E. Raymundo-Piñero and F. Béguin, *J. Power Sources*, 2006, **153**, 183–190.
4 M.-S. Wu and K.-H. Lin, *J. Phys. Chem. C*, 2010, **114**, 6190–6196.
5 J. Schindall, *IEEE Spectrum*, 2007, **44**, 42–46.
6 E. Frackowiak, K. Jurewicz, S. Delpeux and F. Béguin, *J. Power Sources*, 2001, **97–98**, 822–825.
7 M. Hughes, G. Z. Chen, M. S. P. Shaffer, D. J. Fray and A. H. Windle, *Chem. Mater.*, 2002, **14**, 1610–1613.
8 V. Khomenko, E. Frackowiak and F. Béguin, *Electrochim. Acta*, 2005, **50**, 2499–2506.
9 B. Wang, K. Konstantinov, D. Wexler, H. Liu and G. Wang, *Electrochim. Acta*, 2009, **54**, 1420–1425.
10 A. L. M. Reddy and S. Ramaprabhu, *J. Phys. Chem. C*, 2007, **111**, 7727–7734.
11 Z. Fan, J. Chen, K. Cui, F. Sun, Y. Xu and Y. Kuang, *Electrochim. Acta*, 2007, **52**, 2959–2965.
12 V. Gupta and N. Miura, *Mater. Lett.*, 2006, **60**, 1466–1469.
13 P. Sivaraman, V. R. Hande, V. S. Mishra, C. S. Rao and A. B. Samui, *J. Power Sources*, 2003, **124**, 351–354.
14 D. R. Dreyer, S. Park, C. W. Bielawski and R. S. Ruoff, *Chem. Soc. Rev.*, 2010, **39**, 228–240.
15 K. S. Novoselov, A. K. Geim, S. V. Morozov, D. Jiang, Y. Zhang, S. V. Dubonos, I. V. Grigorieva and A. A. Firsov, *Science*, 2004, **306**, 666–669.
16 X. Zhou and Z. Liu, *Chem. Commun.*, 2010, **46**, 2611–2613.
17 D. A. Dikin, S. Stankovich, E. J. Zimney, R. D. Piner, G. H. B. Dommett, G. Evmenenko, S. T. Nguyen and R. S. Ruoff, *Nature*, 2007, **448**, 457–460.
18 C. Petit, M. Seredych and T. J. Bandosz, *J. Mater. Chem.*, 2009, **19**, 9176–9185.
19 S. Park and R. S. Ruoff, *Nat. Nanotechnol.*, 2009, **4**, 217–224.
20 K. A. Mkhoyan, A. W. Contryman, J. Silcox, D. A. Stewart, G. Eda, C. Mattevi, S. Miller and M. Chhowalla, *Nano Lett.*, 2009, **9**, 1058–1063.
21 P. Guo, H. Song and X. Chen, *Electrochem. Commun.*, 2009, **11**, 1320–1324.
22 S.-H. Ng, J. Wang, D. Wexler, K. Konstantinov, Z.-P. Guo and H.-K. Liu, *Angew. Chem., Int. Ed.*, 2006, **45**, 6896–6899.
23 P. G. Xian Du, H. Song and X. Chen, *Electrochim. Acta*, 2010, **55**, 4812–4819.
24 S. Vivekchand, C. Rout, K. Subrahmanyam, A. Govindaraj and C. Rao, *J. Chem. Sci.*, 2008, **120**, 9–13.
25 C. Liu, Z. Yu, D. Neff, A. Zhamu and B. Z. Jang, *Nano Lett.*, 2010, **10**, 4863–4868.
26 M. D. Stoller, S. Park, Y. Zhu, J. An and R. S. Ruoff, *Nano Lett.*, 2008, **8**, 3498–3502.
27 Y. Zhang, H. Li, L. Pan, T. Lu and Z. Sun, *J. Electroanal. Chem.*, 2009, **634**, 68–71.
28 K. S. Kim, Y. Zhao, H. Jang, S. Y. Lee, J. M. Kim, K. S. Kim, J.-H. Ahn, P. Kim, J.-Y. Choi and B. H. Hong, *Nature*, 2009, **457**, 706–710.
29 V. C. Tung, L.-M. Chen, M. J. Allen, J. K. Wassei, K. Nelson, R. B. Kaner and Y. Yang, *Nano Lett.*, 2009, **9**, 1949–1955.
30 D. Cai, M. Song and C. Xu, *Adv. Mater.*, 2008, **20**, 1706–1709.
31 A. Yu, P. Ramesh, X. Sun, E. Bekyarova, M. E. Itkis and R. C. Haddon, *Adv. Mater.*, 2008, **20**, 4740–4744.
32 J. Kim, L. J. Cote, F. Kim, W. Yuan, K. R. Shull and J. Huang, *J. Am. Chem. Soc.*, 2010, **132**, 8180–8186.
33 D. Yu and L. Dai, *J. Phys. Chem. Lett.*, 2010, **1**, 467–470.
34 L. Qiu, X. Yang, X. Gou, W. Yang, Z.-F. Ma, G. G. Wallace and D. Li, *Chem.–Eur. J.*, 2010, **16**, 10653–10658.
35 Z. Liu, J. T. Robinson, X. Sun and H. Dai, *J. Am. Chem. Soc.*, 2008, **130**, 10876–10877.
36 X. Yang, X. Zhang, Z. Liu, Y. Ma, Y. Huang and Y. Chen, *J. Phys. Chem. C*, 2008, **112**, 17554–17558.
37 N. V. Medhekar, A. Ramasubramaniam, R. S. Ruoff and V. B. Shenoy, *ACS Nano*, 2010, **4**, 2300–2306.
38 C. Goómez-Navarro, J. C. Meyer, R. S. Sundaram, A. Chuvilin, S. Kurasch, M. Burghard, K. Kern and U. Kaiser, *Nano Lett.*, 2010, **10**, 1144–1148.
39 B. Krauss, T. Lohmann, D. H. Chae, M. Haluska, K. von Klitzing and J. H. Smet, *Phys. Rev. B: Condens. Matter Mater. Phys.*, 2009, **79**, 165428.
40 D. C. Marcano, D. V. Kosynkin, J. M. Berlin, A. Sinitskii, Z. Sun, A. Slesarev, L. B. Alemany, W. Lu and J. M. Tour, *ACS Nano*, 2010, **4**, 4806–4814.
41 D. Li, M. B. Muller, S. Gilje, R. B. Kaner and G. G. Wallace, *Nat. Nanotechnol.*, 2008, **3**, 101–105.
42 F. M. van der Kooij and H. N. W. Lekkerkerker, *J. Phys. Chem. B*, 1998, **102**, 7829–7832.
43 S. J. Wang, Y. Geng, Q. Zheng and J.-K. Kim, *Carbon*, 2010, **48**, 1815–1823.
44 D. Yang, A. Velamakanni, G. Bozoklu, S. Park, M. Stoller, R. D. Piner, S. Stankovich, I. Jung, D. A. Field, C. A. Ventrice, Jr and R. S. Ruoff, *Carbon*, 2009, **47**, 145–152.
45 W. Gao, L. B. Alemany, L. Ci and P. M. Ajayan, *Nat. Chem.*, 2009, **1**, 403–408.
46 W. Chen, L. Yan and P. R. Bangal, *Carbon*, 2010, **48**, 1146–1152.
47 V. C. Tung, M. J. Allen, Y. Yang and R. B. Kaner, *Nat. Nanotechnol.*, 2008, **4**, 25–29.
48 Z. Wei, D. Wang, S. Kim, S.-Y. Kim, Y. Hu, M. K. Yakes, A. R. Laracuente, Z. Dai, S. R. Marder, C. Berger, W. P. King, W. A. de Heer, P. E. Sheehan and E. Riedo, *Science*, 2010, **328**, 1373–1376.
49 S. Stankovich, D. A. Dikin, R. D. Piner, K. A. Kohlhaas, A. Kleinhammes, Y. Jia, Y. Wu, S. T. Nguyen and R. S. Ruoff, *Carbon*, 2007, **45**, 1558–1565.
50 A. C. Ferrari and J. Robertson, *Phys. Rev. B: Condens. Matter Mater. Phys.*, 2000, **61**, 14095.
51 E. Frackowiak, K. Jurewicz, K. Szostak, S. Delpeux and F. Béguin, *Fuel Process. Technol.*, 2002, **77–78**, 213–219.
52 E. Frackowiak, S. Delpeux, K. Jurewicz, K. Szostak, D. Cazorla-Amoros and F. Béguin, *Chem. Phys. Lett.*, 2002, **361**, 35–41.
53 C. Berger, Z. Song, X. Li, X. Wu, N. Brown, C. Naud, D. Mayou, T. Li, J. Hass, A. N. Marchenkov, E. H. Conrad, P. N. First and W. A. de Heer, *Science*, 2006, **312**, 1191–1196.
54 Y. Chen, X. Zhang, D. Zhang, P. Yu and Y. Ma, *Carbon*, 2011, **49**, 573–580.
55 B. E. Conway, *Electrochemical Supercapacitor: Scientific Fundamentals and Technological Application*, Kluwer Academic/Plenum Publisher, New York, 1999.
56 M. C. Henstridge, E. J. F. Dickinson and R. G. Compton, *Chem. Phys. Lett.*, 2010, **485**, 167–170.
57 P. L. Bonora, F. Deflorian and L. Fedrizzi, *Electrochim. Acta*, 1996, **41**, 1073–1082.
58 T. C. Girija and M. V. Sangaranarayanan, *J. Power Sources*, 2006, **156**, 705–711.
59 P. Yao, P. Chen, L. Jiang, H. Zhao, H. Zhu, D. Zhou, W. Hu, B.-H. Han and M. Liu, *Adv. Mater.*, 2010, **22**, 5008–5012.
60 M. Zhou, Y. Wang, Y. Zhai, J. Zhai, W. Ren, F. Wang and S. Dong, *Chem.–Eur. J.*, 2009, **15**, 6116–6120.
61 Y. Shao, J. Wang, M. Engelhard, C. Wang and Y. Lin, *J. Mater. Chem.*, 2010, **20**, 743–748.